International Journal of GEOMATE, Feb., 2025 Vol.28, Issue 126, pp.80-91
ISSN: 2186-2982 (P), 2186-2990 (O), Japan, DOI: https://doi.org/10.21660/2025.126.4779
Geotechnique, Construction Materials and Environment

GEOMETRY AND KINEMATICS OF THE RENUN SEGMENT OF THE SUMATRAN FAULT IN NORTH SUMATRA

Dimas Didik Prayogo[1,3], *Gayatri Indah Marliyani[2], and Nugroho Imam Setiawan[2]

[1]Master Program in Geological Engineering, Gadjah Mada University, Yogyakarta, Indonesia;
[2]Department of Geological Engineering, Gadjah Mada University, Yogyakarta, Indonesia;
[3]Agency for Meteorology Climatology and Geophysics (BMKG), Alor Geophysics Station, Indonesia

*Corresponding Author, Received: 28 Oct. 2024, Revised: 16 Nov. 2024, Accepted: 24 Nov. 2024

ABSTRACT: The Sumatra region hosts shallow active faults, including the Sumatran Fault, resulting from oblique convergence between the Indo-Australian and Eurasian plates. This condition contributes to high earthquake activity in Sumatra, including the North Sumatra region. Recent seismic activity, a moment magnitude (Mw) 6.0 along the Renun Fault in North Tapanuli, North Sumatra, occurred on October 1, 2022. This event, followed by 124 aftershocks, highlights the seismic hazard posed by this fault. This research aims to characterize the geometry and kinematics of active faults along the Renun Fault to update the existing earthquake hazard maps for the North Sumatra region. In this study, we employ earthquake relocation and focal mechanism methods to analyze the earthquake distribution pattern and focal mechanism solutions, along with tectonic-geomorphological analysis of the Renun Fault. The focal mechanism solution indicates a dominant dextral strike-slip faulting mechanism. Analysis of the focal mechanism solutions and tectonic-geomorphological features using remote sensing reveals a dominant movement direction of the fault, from northwest to southeast (NW-SE). Based on the surface geometry, we propose that the Renun Segment can be further divided into three subsegments: Renun-A (with a length of ~187.3 km), Renun-B (with a length of 33.8 km), and Renun-C (with a length of 25.2 km), with estimated maximum magnitudes of Mw 7.74, 6.52, and 6.31, respectively.

Keywords: Renun fault, Double difference, Focal mechanism, Tectonic-geomorphology, Moment magnitude

1. INTRODUCTION

Sumatra Island is located in a convergence zone between two plates: the Indo-Australian plate, which subducts beneath the Eurasian plate, creating a subduction zone and triggering earthquakes [1,2]. Moreover, many areas in the Sumatra region are dissected by shallow active faults, among them is the Sumatra Fault Zone (SFZ), which accommodating the horizontal component of the oblique convergence between the Indo-Australian and Eurasian plates [3]. Consequently, this geological configuration results in heightened seismic activity in Sumatra, including occurrences in the North Sumatra region [4].

The North Sumatra region is notorious for its susceptibility to earthquakes, marked by a historical series of destructive events. Since most of these events happened tens or more than a century ago, gathering data connected to historical records is challenging because most currently available earthquakes were not fully documented at the time [5]. There are at least four earthquakes recorded based on historical records, such as 1861, 1873, 1892 and 1921 [6]. The 1861 earthquake was felt in Tapanuli and Sibolga with an intensity of VII-IX Modified Mercalli Intensity (MMI) and caused many houses to collapse and a tsunami (observed in Singkil, Nias, and Tello). Furthermore, in 1873, an earthquake was felt in Mandailing (with an intensity of VI MMI) and Tapanuli (with an intensity of VI MMI), causing many houses and bridges to be damaged. Nineteen years later, in 1892, an earthquake was felt in Parapat (with an intensity of VI MMI), seriously damaging three buildings. Furthermore, the 1921 earthquake was estimated to have a magnitude of ~M 7.0 based on the radius of the resulting shock [3,5,7]. Moreover, in 1965, seismographs recorded an earthquake M 5.3, causing damage to brick buildings and landslides [6]. Additionally, both the Agency for Meteorology, Climatology, and Geophysics (BMKG) [8] and the United States Geological Survey (USGS) [9] documented a M 6.0 quake in 1987, claiming the lives of 2 individuals, injuring 22 and causing extensive damage to over 300 buildings. Moreover, the North Tapanuli area experienced significant seismic events in 1984 and 2011. The 1984 tremor, measuring M 5.1, left 123 people injured, collapsing four school buildings, severely damaging another, and causing cracks in three government buildings [10]. Subsequently, a moment magnitude (Mw) 5.5 happened in 2011, damaging 165 houses [10]. These occurrences highlight the seismic hazards associated with activity along the Sumatran Fault, including the Renun segment in the North Sumatra region [5].

Earthquakes in the North Sumatra region typically occur at a depth of less than 40 km and exhibit a characteristic distribution pattern. According to the BMKG earthquake catalog starting from 2010 until 2022 [8], a significant earthquake measuring Mw 6.0 struck the North Tapanuli area of North Sumatra on

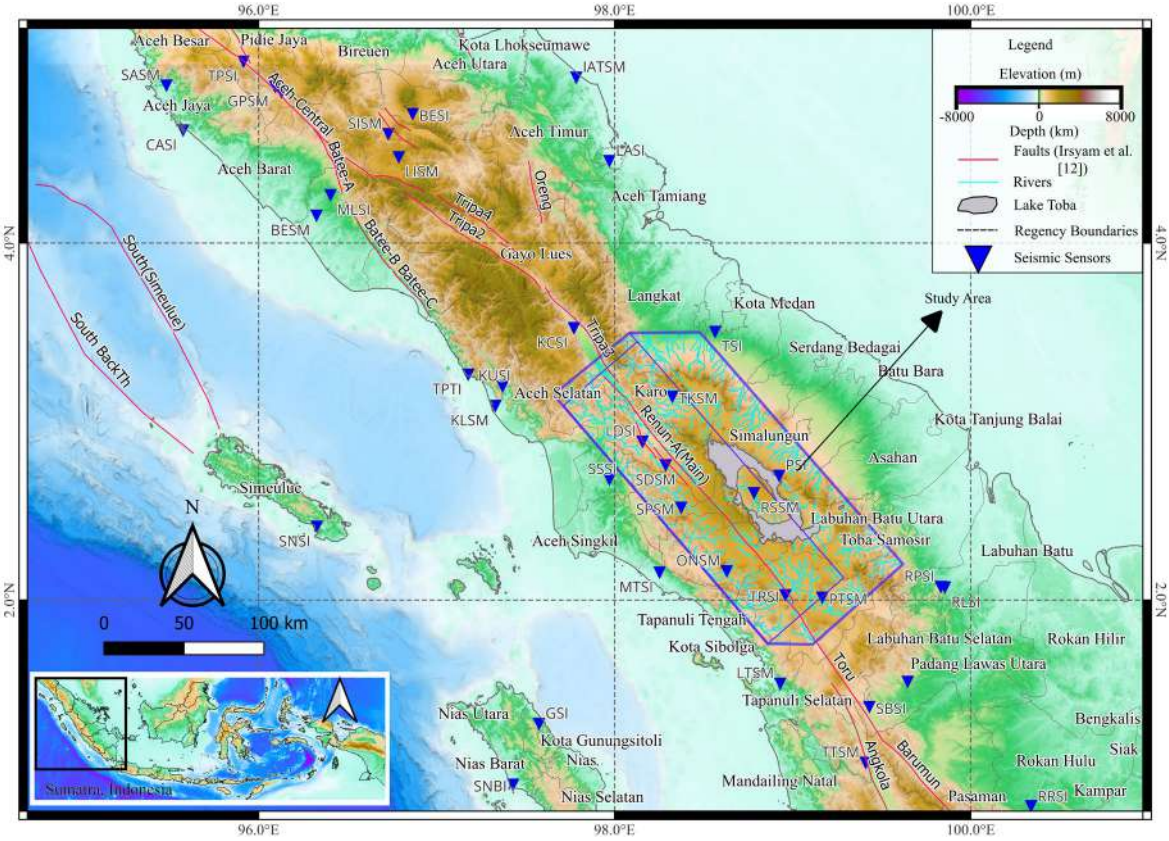

Fig. 1 Distribution map of BMKG seismic sensors within a 500 km radius from North Sumatra, Indonesia, overlaid on a base map sourced from [11]. The fault data (depicted in red) were acquired from prior research [12].

aftershocks. Three large aftershocks with magnitudes greater than M 5.0 were recorded. The aftershock distribution was irregular, primarily distributed within a 50 km zone. We conduct a thorough analysis and quality control of earthquake parameters in the North Sumatra region using data obtained from regional BMKG seismometers. The result will help us understand the earthquake characteristics, particularly the detailed geometry of the fault. Furthermore, we integrated this seismic data with geophysical information [13], including anomalous values of P-wave (Vp) and S-wave (Vs) velocities, along with the pattern of Vp/Vs values in area close to the Toba Caldera.

Active faults often leave visible marks on the Earth's surface and are recognized by unique topography, such as scarps or linear arrangements of geological features [14]. Understanding which areas are traversed by active faults aids researchers and government agencies in mapping out fault traces for effective disaster mitigation strategies and influencing building codes. While active fault lines in Sumatra have been extensively studied [3,5,15], It is essential to characterize the geometry and kinematics of the Renun Fault based on the latest earthquake records and topographic data with better resolution to improve the quality of the remotely-based tectonic geomorphology mapping.

This research aims to characterize the geometry and kinematics of active faults along the Renun Fault to update the existing seismic hazard maps for the North Sumatra region. Our results will provide additional parameter data for Seismic Hazard Analysis (SHA), such as fault geometry (length and width), fault kinematics, and Mw. In turn, this will increase the quality of seismic hazard assessment in the area, enabling effective disaster mitigation strategies and influencing building codes.

This active fault map utilized multiple approaches, including remotely-based tectonic geomorphology mapping (hillshade, slope, and aspect), seismicity distribution by relocating existing earthquake data from the BMKG catalog, and analysis of focal mechanisms. The distribution of earthquakes reveals specific clusters, indicating the presence of active faults on land while also considering the alignment of the geomorphological map. The conclusions drawn from this research expand our knowledge and deepen our understanding of the Renun Fault System.

2. GEOLOGY OF THE STUDY AREA

The geology of the Renun Fault Zone has been mapped in multiple 1:250,000 geological maps of

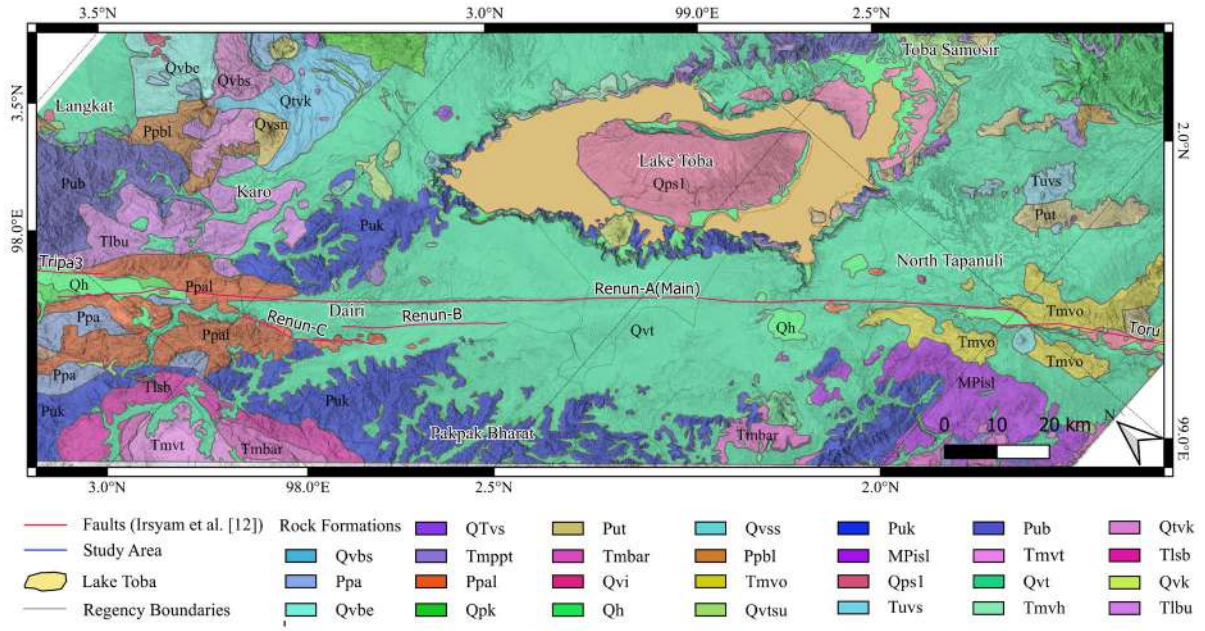

Fig. 2 Geological map of North Sumatra, Indonesia, modified from the regional geological map of the Sidikalang and parts of Sinabang [16], the Medan [17], the Pematangsiantar [18], and the Padangsidempuan and Sibolga [19], and Indonesia Geospatial [20] with base map from National Seamless Digital Elevation Model and Bathymetry (DEMNAS) [21].

North Sumatra covering areas including Sidikalang and parts of Sinabang [16], Medan [17], Pematangsiantar [18], and Padangsidempuan and Sibolga [19] regions.

The Renun Fault Zone dissects various lithology, predominated by Miocene-Holocene volcanic, sedimentary rocks and loose sediments (Fig. 2). The lithological units found in the area including the Toba Tufa Formation (Qvt), Sibutan Unit (Qvtsu: rhyolitic lavas and pyroclastic), Singkut Unit (Qvbs: andesites, dacites, microdiorites, and tuffs), Bekulap Unit (Qvbe: dacitic pyroclastic and lavas), Pusat Kembar (Qvk: andesites, dacites, basalts, and pyroclastics), Takur-takur Unit (QTvk: andesites, dacites, and pyroclastics), Symbolon Unit (QTvs: andesites lavas, plugs, and pyroclastics), and Alas Formation (Ppal and Ppa). Furthermore, Holocene-Miocene sedimentary rock types comprise alluvium (Qh), Sibolga Formation (Tlsb), Peutu Formation (Tmppt), Kluet Formation (Puk: metaquartzose arenites, metawackes, slates, and phyllites), Bahorok Formation (Pub), and Kutacene Formation (Qpk) covering the eastern and western parts of North Sumatra. Additionally, intrusive rocks from the Palaeozoic era manifest as granite, diorite, aplite, and pegmatite (MPisl) cropped in various locations across North Tapanuli. Metamorphic rocks, such as limestone (marble and limestone schist), dating back to the Palaeozoic era, dominate Karo Regency and its surroundings. The west coast is characterized by sedimentary rocks, including sandstone and clay, interspersed with several layers of limestone [16-19,22].

3. DATA AND METHODS

We utilized 8-m resolution Digital Elevation Model (DEM) data (and its derived maps) from DEMNAS [21] for remotely-based tectonic geomorphology mapping. Subsequently, a shaded-relief map of the Renun Fault was generated using Quantum Geographic Information System (QGIS) software (freely obtained from [23]), accompanied by a shadow map created with virtual solar lighting positions derived from various solar azimuth directions. The breaks in topographic variations serve as crucial indicators for delineating surface features that may indicate surface projection of active fault.

3.1 Remotely-based Tectonic Geomorphology Mapping

We analyze the slope [24] and aspect to map any linear break that may indicate active faults. Active faults typically exhibit consistent slope breaks [25]. We identify geomorphic indications of active faulting, including the presence of young fault scarps, displacement of young geomorphic features such as river terraces and channels, and deformation of recent sediments [26].

We also map any discontinuity that may act as a barrier to earthquake rupture. Rupture termination may be significantly influenced by the size of

geometrical discontinuities relative to the rupture length. Generally, when the discontinuity between fault traces is less than 3–4 km, there remains the possibility of interconnected relationships between the individual faults [27-28].

3.2 Hypocenter Relocation

The earthquake data analyzed in this research comprise the International Seismological Centre (ISC) earthquake catalog [29] and BMKG data obtained from seismometers positioned within a less than 500 km radius around the Renun Fault. This data includes earthquake catalog information, arrival times, and waveforms [8]. ISC conducts quality control on their data, resulting in a small Root Mean Square (RMS) error from 1960 to 2009. Additionally, BMKG data from 2010 to 2022, specifically earthquake arrival time data, is used during the earthquake relocation process to enhance the accuracy of earthquake parameter determination. BMKG employs the Locator in SeisComP (LocSAT) program [30], a component of SeisComP3, to facilitate the testing and acquisition of arrival time data for this study. Furthermore, the local speed model parameters utilized during the relocation stage were derived from prior research [31]

During the relocation process, 863 earthquakes, ranging in Mw from 1.2 to 6.0, were identified from 10,801 primary wave arrivals and 2,781 secondary wave arrivals recorded by 66 monitoring stations. Subsequently, the HypoDD program [32], which employs the double-difference method [33], was used to relocate earthquakes occurring between 2010 and 2022, including mainshocks and aftershocks within a specified timeframe. The double-difference method assumes that if the hypocentral distance between two earthquakes is shorter than the distance from the recording station, both earthquakes share the same medium along the ray path.

3.3 Focal Mechanism Analysis

We utilized the Kinematic Waveform Inversion (Kiwi) tools [34], which follow the guidelines from [35-36], to determine the focal mechanism solutions. This inversion process primarily utilized long waves, which are less susceptible to perturbations from unknown small-scale heterogeneities in the Earth's structure [36]. We selected four earthquakes with a maximum distance of less than 300 km from the recording station to the epicenter and an Mw exceeding 4.0. The input data comprised BMKG waveform data with three components (vertical, north-south, and east-west), utilizing the International Association of Seismology and Physics of the Earth's Interior Seismic Travel Time Model 1991 (IASP91) [37]. To achieve optimal results in point-source inversion, we applied various low-frequency band-pass filters ranging from 0.006 Hz to 0.077 Hz, aiming to minimize misfits.

3.4 Estimation of Maximum Magnitude

We follow empirical relationship to estimate the maximum earthquake of Mw, Gunawan [38] compared the scale relationship between earthquake magnitude and rupture length using data from the latest earthquakes in Indonesia. As per the equation proposed by Cheng et al. [39] for dip-slip and strike-slip faults, the results exhibited smaller misfit values than other scale relationships. Hence, their formulation appears more suitable for earthquakes occurring in Indonesia. We use the equation of Cheng et al. [39] at the strike-slip fault, where L is the fault length in km, as follows:

$$Mw = (\log L + 2.45)\,/0.61 \quad (1)$$

4. RESULTS AND DISCUSSIONS

We analyze the 8-m resolution digital elevation model from DEMNAS to map linear features that may be associated with faulting. Our observation indicates a dominant lineament pattern in the NW-SE direction. While the identified lineaments, in general, are unaffected by changes in lithological contacts (such as in the Karo, Dairi, and North Tapanuli areas in Fig. 2 for location), some lineaments align closely with lithological boundaries, which may indicate that the lineaments are controlled by lithology contrast to erosion, although lithological contrast may also indicate fault contact.

Figure 3 shows an example of lineament mapping using DEMNAS data with their derivative maps. The slope, aspect, and hillshade maps (Figs. 3a, 3b, and 3c) highlighted morphological features such as deflected channels, push-up ridges, sag ponds, and linear valleys along the fault (shown by the black arrow in Fig. 3c). Hence, the systematic changes of these orientation may indicate fault, as shown in Fig. 3d.

From the total of 863 earthquakes we analyzed, 804 were successfully relocated at the relocation stage. The other 59 events did not meet the criteria for parameterization during the HypoDD process. We compared BMKG earthquake parameters before and after relocation by mapping the distribution of earthquakes (Figs. 5b and 5c) and creating cross-sections perpendicular to the Renun Fault at distances of 4 km and 2 km, as well as cross-sections HH-HH' (Figs. 4c and 4d), aligned with the Renun Fault direction. The distribution of relocated earthquakes in the Renun Fault Zone, as depicted in Figures 5b and 5c, exhibits a distinct pattern. This pattern reveals a correlation among three earthquake events: February 28, 2010, February 24, 2018, and October 1, 2022.

On February 28, 2010, a main earthquake with a

local magnitude (MLv) of 5.0 occurred in the North Tapanuli area, followed by 25 aftershocks. Generally, the earthquake distribution pattern is concentrated along the Renun Fault in North Tapanuli, corresponding to the latest earthquake on October 1, 2022, with an Mw of 6.0. The distribution of earthquakes in 2010 and 2022 is irregularly concentrated within a 50 km area. The earthquake on February 24, 2018, with an Mw of 4.7, followed by 12 aftershocks, also occurred in North Tapanuli, and its distribution aligns with the locations of the 2010 and 2022 earthquakes. Furthermore, shallow earthquake activity less than 25 km deep is observed in the Toba Caldera, and other earthquakes are delineated along the Renun Fault.

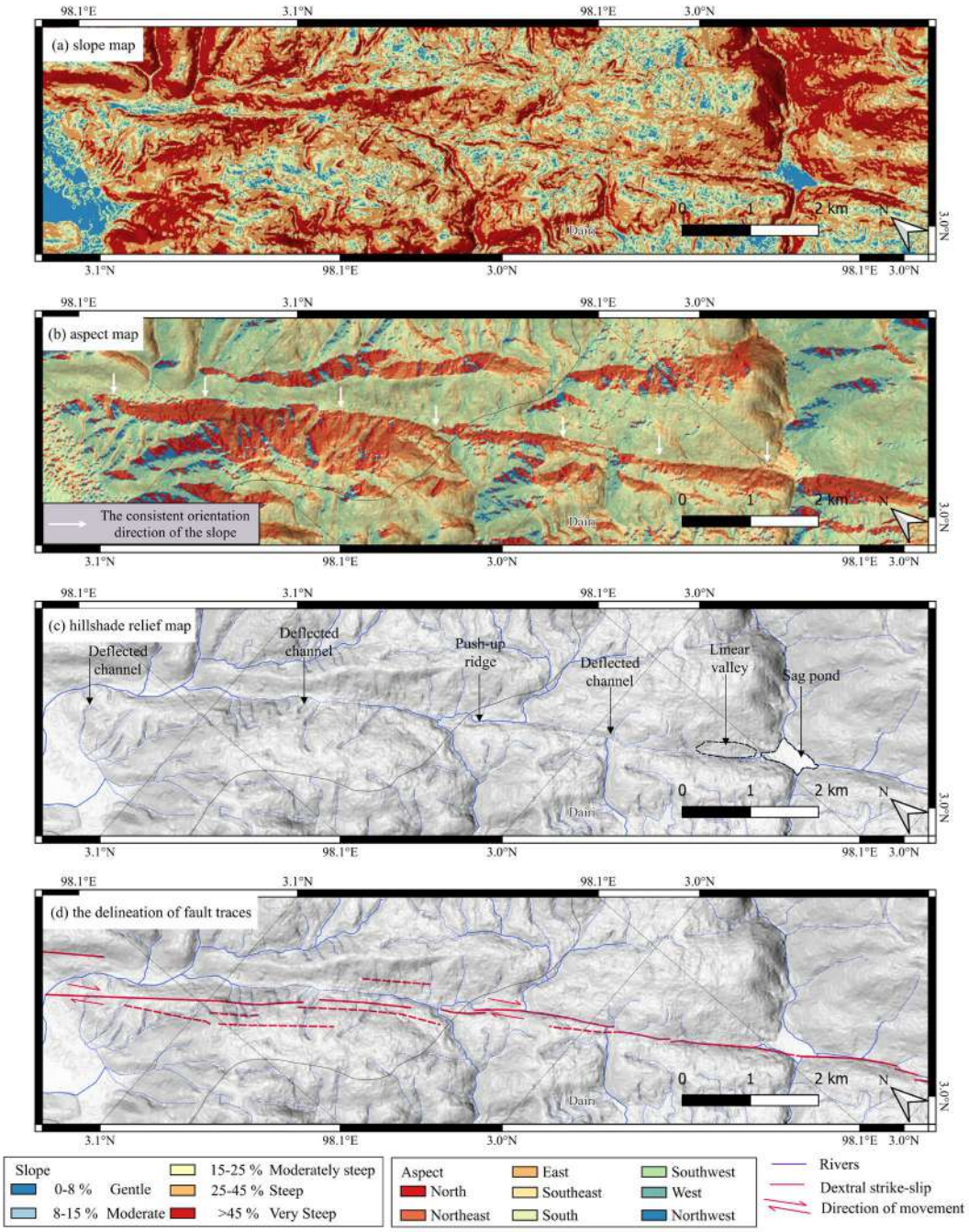

Fig. 3 Examples of derivative maps used to delineate fault traces include (a) slope, (b) aspect, and (c) hillshade (see Fig. 5a for location). Morphological features such as deflected channels, push-up ridges, sag ponds, and linear valleys are identifiable through these maps. (d) the delineation of fault traces on the hillshade, red line indicates fault interpretation results from this study, and dashed lines for secondary fault traces. The base maps from 8-m resolution DEMNAS (this resolution is adequate for mapping fault traces in detail) [21].

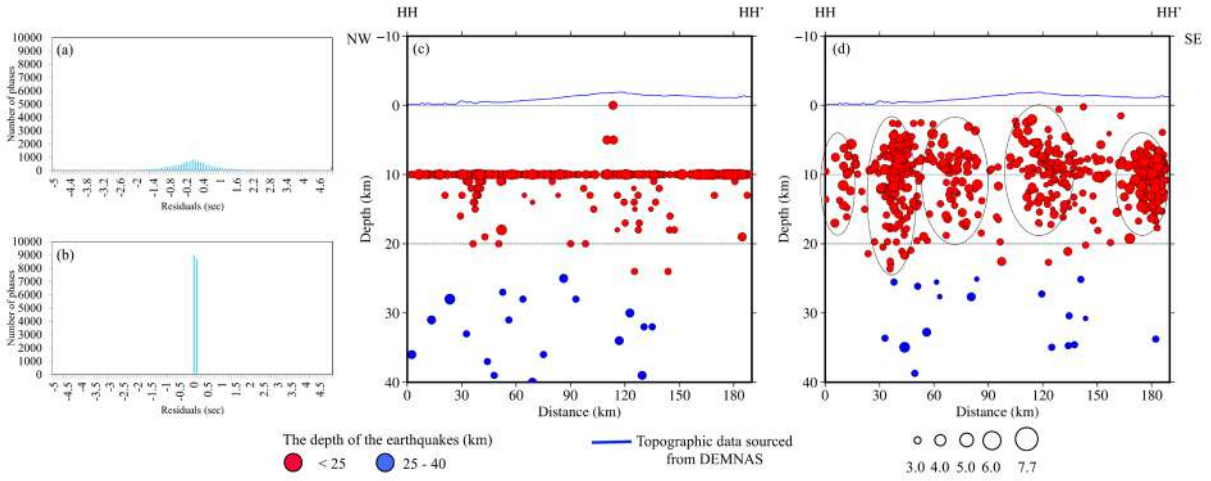

Fig. 4 Residual time histograms: (a) before and (b) after relocation. Earthquake distribution: (c) before and (d) after relocation from 2010 to 2022 with cross-section HH-HH' (NW-SE) is shown in Figs: 5b and 5c (yellow cross-section).

This earthquake distribution pattern indicates the presence of the Renun Fault in the seismogenic zone (assuming a depth of ~20 km), where most of the earthquake distribution occurs at depths ranging from 0 to 25 km. The histogram (Fig. 4b) shows a better traveltime residual value, while the histogram after relocation hypocenter produces a residual value closer to zero than before the relocation (Fig. 4a). Cross-section results in a northwest-southeast (NW-SE) direction, as shown in Fig. 4c, indicate that the majority of earthquake distribution in the BMKG catalogue is at a depth of 10 km. The relocation results demonstrate successful distribution according to depth (Fig. 4d) as well as in Fig. 6 (cross-section distance 4 km) and Fig. 7 (cross-section distance 2 km) in a northeast-southwest (NE-SW) direction. Thus, earthquakes occurring at shallow depths are predominantly located within rocks in the Earth's crust, possessing heterogeneous properties and prone to brittle failure at depths of less than 20 km. Additionally, focal mechanism solutions were determined for four earthquakes occurring at shallow depths. The misfit between observed and synthesized traces after inversion for both the mainshock and aftershock focal mechanisms ranges from 0.3 to 0.5 for three out of four earthquakes, indicating an acceptable match according to the criterion outlined in [36]. Consequently, this study's focal mechanism results that used regional data (more seismic sensors) align with the Global Centroid Moment Tensor (GCMT), which predominantly exhibits a dextral strike-slip mechanism along the Renun Fault [40]. Three of the four selected earthquakes analyzed from 2010 to 2022 (event numbers 2, 5, 6, and 7 in Fig. 5a) displayed a dextral strike-slip focal mechanism (refer to Table 1). Similarly, seven earthquakes from the GCMT dataset (refer to Table 1) exhibited a dextral strike-slip focal mechanism. These findings collectively suggest that movement along the Renun Fault predominantly follows a dextral strike-slip mechanism in an NW-SE direction.

We overlay the focal mechanism solution with the distribution of relocated earthquakes and create an arbitrary line projecting each of the solution planes to the surface profile in the cross-section depth profile. Within the depth profile, a discernible pattern emerges in the distribution of earthquakes that closely aligns with the focal mechanism plot. This alignment is illustrated by projecting the dip angle (depicted as a dashed line) onto the surface, marked with a blue inverted triangle. These projection lines can be used to guide the search for the surface manifestation of the fault plane [41]. Examining the cross-section with a distance of 4 km (line AB-AB' in Fig. 5b) and illustrated with depth in Fig. 6, the focal mechanism plot, along with its dotted line projection, correlates with the distribution of earthquakes observed across cross-sections AC-AC', AD-AD', and AE-AE' in Figures 5b and 6. Additionally, within the AQ-AQ' cross-section, the distribution pattern of the focal mechanism dip projection follows that of the AP-AP' cross-section. In contrast, the AV-AV' cross-section aligns with the projection line in the AU-AU section. Furthermore, the AO-AO', AR-AR', AS-AS', and AT-AT' cross-sections exhibit matching dip trends with each focal mechanism displayed in the cross-section.

Similarly, examining the cross-section with a distance of 2 km (Fig. 5c) and illustrated with depth in Fig. 7, the earthquake distribution pattern in the CG-CG' section corresponds to the dip projection of the CF-CF' focal mechanism. Moreover, cross-sections CH-CH' and CJ-CJ' correlate with cross-section CI-CI', while cross-section CK-CK' aligns with the projection of the focal mechanism line CL-CL'. Additionally, the geometric shape of the earthquake distribution pattern in CM-CM' corresponds to the cross-section in CN-CN'.

Below the Toba Caldera, the earthquakes extend

to a depth of 45 km (Fig. 5b and cross-sections AB-AB', AC-AC', AD-AD', and AE-AE' in Fig. 6). These cross-sections are situated below Mount Pusuk Buhit, and the surrounding area exhibits low Vp and Vs anomaly values and high Vp/Vs values [13]. These patterns may indicate typical characteristics of dynamic processes in the magma chamber beneath a volcano, where the movement of liquid magma may generate fractures and be associated with seismic activity. The intrusion of fluids and magma beneath the volcano can trigger brittle faults and heightened seismicity on faults (Fig. 5b and cross-sections AB-AB', AC-AC', AD-AD', and AE-AE' in Fig. 6 are depicted in orange earthquakes), consistent with complex volcanic conditions.

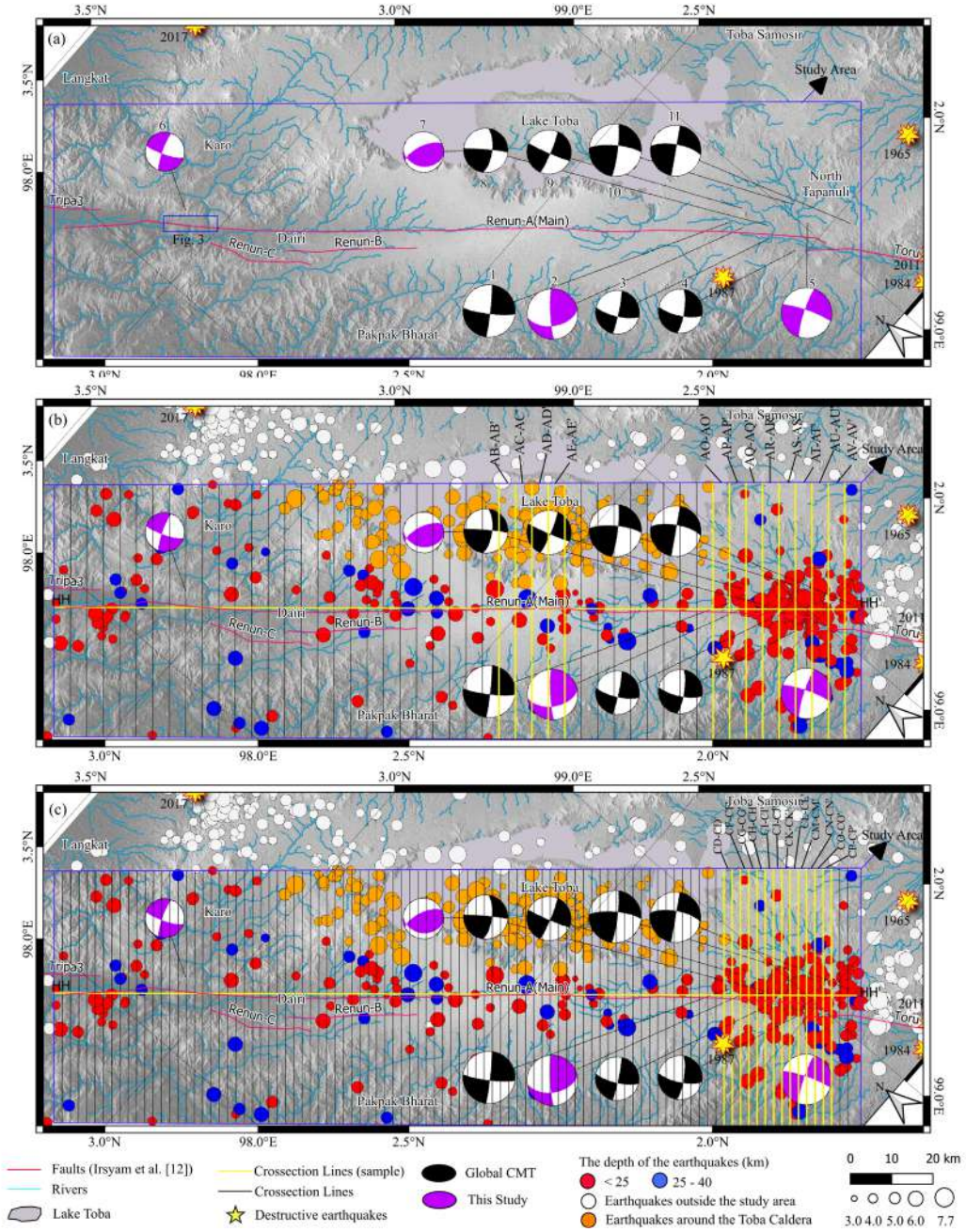

Fig. 5 Map displaying focal mechanism processing results (featuring projections from the upper hemisphere) with Kiwi (depicted in purple) and GCMT (depicted in black) [40]. Subfigures include (a) the focal mechanism alone; (b) the focal mechanism alongside seismicity, with cross-sections provided every 4 km; and (c) the focal mechanism alongside seismicity, with cross-sections provided every 2 km. The yellow cross-section represents a sample from this study, with the 4 km and 2 km cross-sections further detailed in Figs. 6 and 7, respectively.

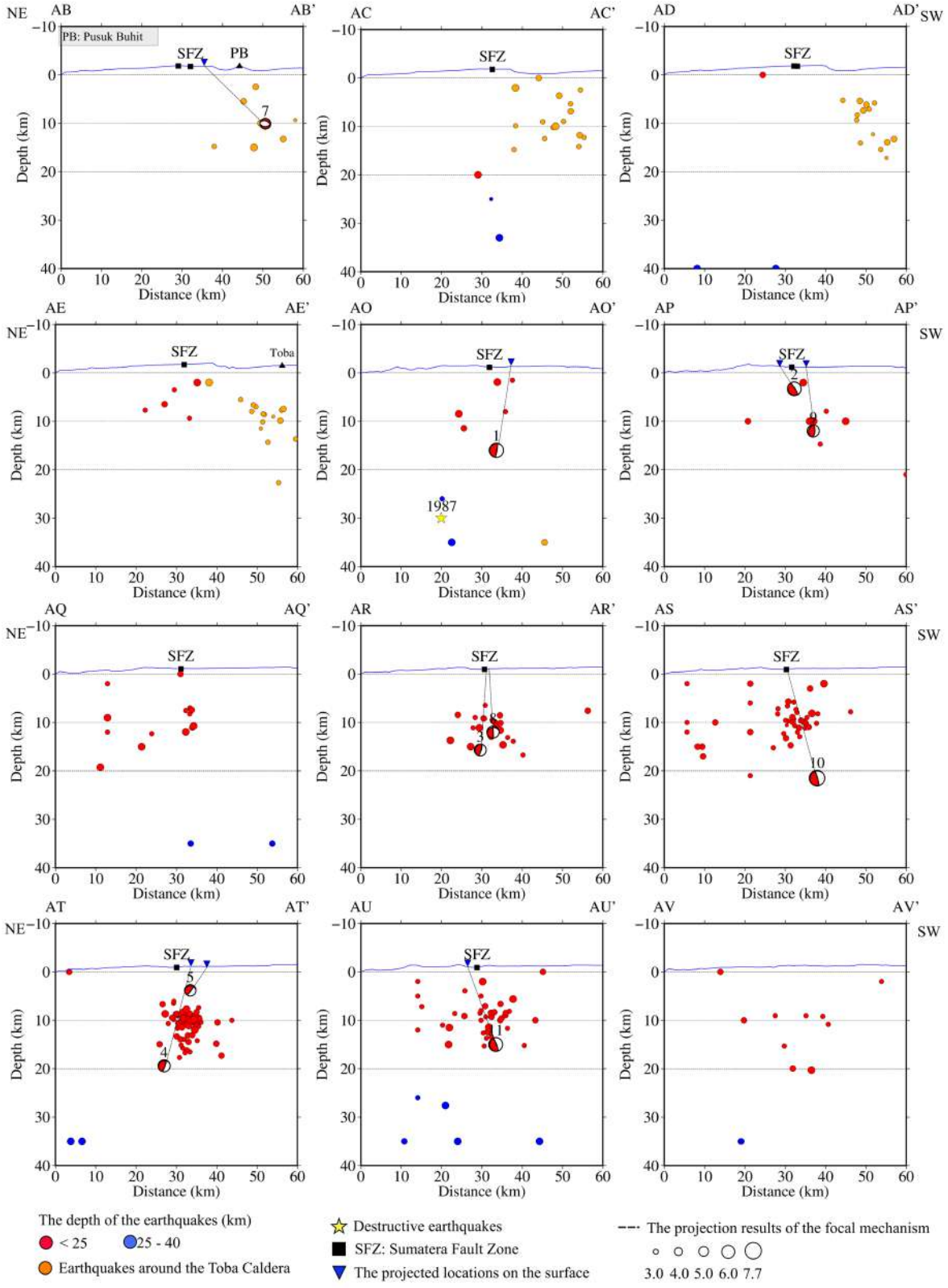

Fig. 6 Cross-section results depicting the depth profile of each earthquake after relocation, alongside focal mechanism projection results from the lower hemisphere, with cross-sections spaced 4 km apart. Dashed lines illustrate the projection results of the focal mechanism solution on the surface, with blue triangles indicating the projected locations on the surface. Topographic data (depicted in blue line) sourced from 8-m resolution DEMNAS [21].

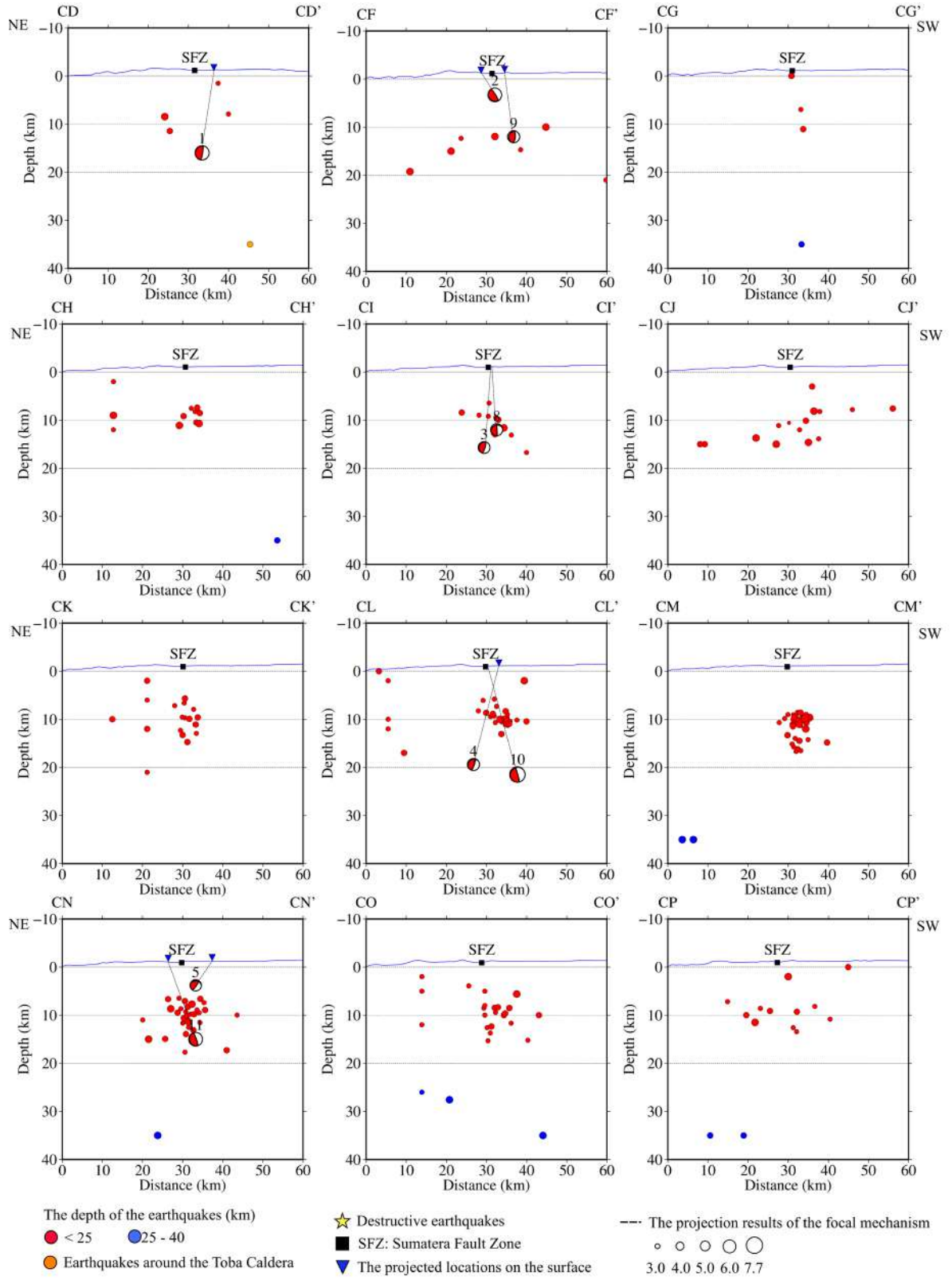

Fig. 7 Cross-section results displaying the depth profile of each earthquake after relocation, along with focal mechanism projection results from the lower hemisphere, with cross-sections spaced 2 km apart. Dashed lines indicate the projection results of the focal mechanism solution on the surface, while blue triangles denote the projected locations on the surface. Topographic data (depicted in blue line) sourced from 8-m resolution DEMNAS [21].

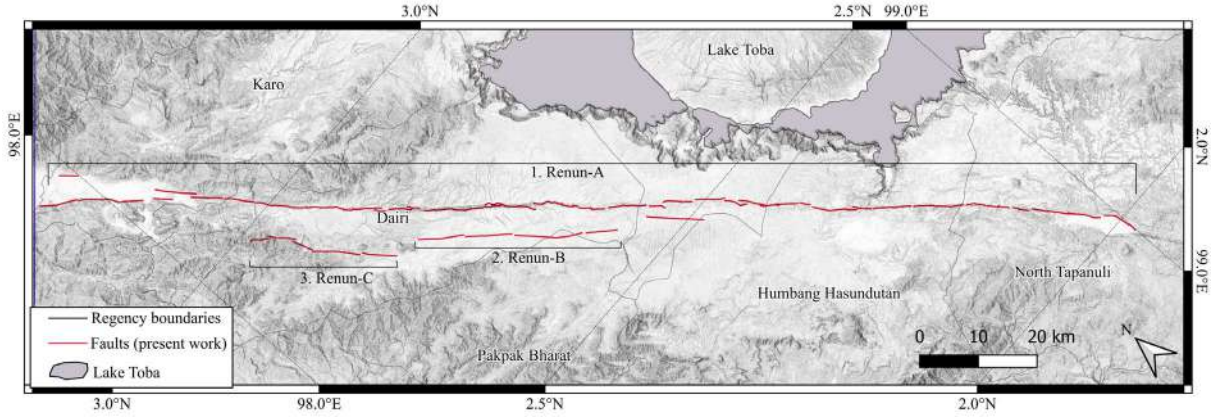

Fig. 8 Map showing the Renun Fault interpretation results from this study, we divided the Renun Fault into three subsegments: Renun-A, Renun-B, and Renun-C. The base map from DEMNAS [21].

Table 1 Results of the focal mechanism of earthquakes around the Renun A, Renun B, and Renun C faults.

ID	Date, Time (UTC)	Lat., Lon.	Depth (km)	Mw	Strike (°), Dip (°), Rake (°)	f (Hz)	Sense Mechanism
	present work						
2	30/09/2022, 20:54:16	2.14°N, 98.91°E	3.3	5.7	235°,84°,-32°/ 329°,58°,-173°	0.016-0.048	Dextral strike-slip
5	06/10/2022, 20:00:43	2.04°N, 99.01°E	3.8	4.7	48°,69°,-37°/ 153°,56°,-155°	0.007-0.051	Dextral strike-slip
6	16/02/2015, 15:11:10	3.08°N, 98.14°E	7.9	3.9	72°,87°,156°/ 163°,66°,3°	0.006-0.077	Dextral strike-slip
7	05/7/2013, 16:54:40	2.65°N, 98.68°E	10.1	4.4	28°,47°,77°/ 227°,44°,104°	0.009-0.049	Thrust
	GCMT						
1	30/09/2022, 19:28:43	2.17°N, 98.9°E	16.0	5.8	146°,81°,-176°/ 55°,86°,-9°	-	Dextral strike-slip
3	06/10/2022, 20:00:45	2.08°N, 98.93°E	15.7	4.9	152°,74°,-176°/ 61°,86°,-16°	-	Dextral strike-slip
4	24/02/2018, 10:02:35	2.02°N, 98.95°E	19.4	5.0	152°,72°,-165°/ 57°,76°,-18°	-	Dextral strike-slip
8	30/09/2022, 20:37:41	2.1°N, 98.95°E	12.0	4.9	56°,66°,4°/ 324°,86°,156°	-	Dextral strike-slip
9	30/09/2022, 19:50:41	2.17°N, 98.94°E	12.0	4.9	72°,83°,-4°/ 162°,86°,-173°	-	Dextral strike-slip
10	25/04/1987, 19:22:13	2.09°N, 99.02°E	21.5	6.4	324°,75°,172°/ 56°,83°,15°	-	Dextral strike-slip
11	28/04/1987, 15:32:33	1.97°N, 99.07°E	15.0	5.7	329°,70°,180°/ 59°,90°,20°	-	Dextral strike-slip

Note: This table is based on the focal mechanism solution in Fig. 5a

Table 2 Mw estimation calculations in this study

Id	Subsegment	Length (km)	Mw
1	Renun-A	187.3	7.74
2	Renun-B	33.8	6.52
3	Renun-C	25.2	6.31

Note: Mw was calculated using an equation by Cheng et al. [39]

Based on the mapping and also supported by the analysis of the seismicity pattern, we came up with our refined interpretation of the fault traces, as shown in Fig. 8. We divide the Renun Fault Zone into several fault strands based on their geometrical discontinuity at the surface. We separate the fault zone into three subsegments: Renun-A with a length of ~187.3 km, Renun-B with a length of 33.8 km, and Renun-C with a length of 25.2 km (Fig. 8). Based on their total length, we estimate the maximum magnitude that may occur along these faults using an empirical relationship by Cheng et al. [39]. The estimated maximum magnitudes of the Renun A, B, and C are Mw 7.74, 6.52, and 6.31, respectively (Table 2).

5. CONCLUSION

We have conducted earthquake relocation and focal mechanism analysis and used their distribution correlation to understand the geometry of the Renun Fault. Our findings suggest that the Renun Fault is a dextral strike-slip fault oriented to the NW-SE direction. Furthermore, using remote sensing, our observation of tectonic-geomorphological features indicates a dominant lineament pattern in the NW-SE

direction. These lineaments facilitated the interpretation of surface faults, allowing for the reformation of the Renun Fault into three subsegments: Renun-A (with a length of ~187.3 km), Renun-B (with a length of 33.8 km), and Renun-C (with a length of 25.2 km). We estimate that the Renun-A, Renun-B, and Renun-C may be capable of producing earthquakes with maximum magnitudes of Mw 7.74, 6.52, and 6.31, respectively.

This research provides evidence of the active traces of the Renun Fault and provides insight into their complex geometry and segmentation. To better understand recent activity and its pattern in further research, incorporating more comprehensive seismic data or deploying seismic sensors to capture smaller-magnitude earthquakes can help fill gaps in the seismicity data, thereby improving the accuracy of subsurface profile delineation. Moreover, the utilization of higher-resolution topographic data, such as Light Detection and Ranging (LiDAR) data, may significantly improve the geomorphological tectonic analysis and can greatly enhance the accuracy of interpreting active faults at the surface.

6. ACKNOWLEDGMENTS

The author would like to extend gratitude to the Earthquake and Tsunami Centre of BMKG for their support in providing data availability. Finally, heartfelt thanks are due to the Human Resource Development Centre of MKG (PPSDM MKG) for their generous provision of research funding. In addition, we created figures for this study using QGIS software and Generic Mapping Tools (GMT).

7. REFERENCES

[1] McCaffrey R., The Tectonic Framework of the Sumatran Subduction Zone, Annu Rev Earth Planet Sci, vol. 37, no. 1, 2009, pp. 345–366.

[2] Richards S., Lister G., and Kennett B., A Slab in Depth: Three-Dimensional Geometry and Evolution of the Indo-Australian Plate, Geochemistry, Geophysics, Geosystems, vol. 8, no. 12, 2007, p. 12003.

[3] Sieh K., and Natawidjaja D., Neotectonics of the Sumatran Fault, Indonesia, J Geophys Res Solid Earth, vol. 105, no. B12, 2000, pp. 28295–28326.

[4] Simanjuntak A., Muksin U., Asnawi Y., Rizal S., and Wei S., Recent Seismicity and Slab Gap Beneath Toba Caldera (Sumatera) Revealed Using Hypocenter Relocation Methodology, International Journal of GEOMATE, vol. 23, no. 99, 2022, pp. 82–89.

[5] Natawidjaja D. H., The Sumatran Fault Zone - From Source to Hazard, Journal of Earthquake and Tsunami, vol. 1, no. 1, 2007, pp. 21–47.

[6] Soetardjo, Untung M., Arnold E. P., Soetadi R., Ismail S., and Kertapati E. K., Southeast Asia Association of Seismology and Earthquake Engineering Series on Seismology Volume V - Indonesia, Jakarta, 1985, pp. 1–206.

[7] Daryono M. R., Natawidjaja D. H., and Sieh K., Twin-Surface Ruptures of the March 2007 M > 6 Earthquake Doublet on the Sumatran Fault, Bulletin of the Seismological Society of America, vol. 102, no. 6, 2012, pp. 2356–2367.

[8] Agency for Meteorology Climatology and Geophysics (BMKG), InaTEWS E. Repository, 2023, https://repogempa.bmkg.go.id.

[9] United States Geological Survey (USGS), Significant Earthquakes - 1987, 2023, https://earthquake.usgs.gov.

[10] Setiyono U., Gunawan I., Priyobudi, Yatimantoro T., Imananta R. T., Ramadhan M., Hidayanti, Anggraini S., Rahayu R. H., Hawati P., Yogaswara D. S., Julius A. M., Apriani M., Harvan M., Simangunson G., and Kriswinarso T., Catalog of Significant and Damaging Earthquakes 1821-2018, Earthquake and Tsunami Center, Jakarta, 2019, pp. 1-280 (in Indonesian).

[11] General Bathymetric Chart of the Oceans (GEBCO), Gridded Batymetry Data, 2023, https://download.gebco.net.

[12] Irsyam M., Widiyantoro S., Natawidjaja D. H., Meilano I., Rudyanto A., Hidayati S., Triyoso W., Hanifa N., Djarwadi D., and Faizal L., National Earthquake Study Centre (PuSGeN), Research Centre for Housing and Human Settlement, Directorate General for Research and Development, Ministry of Public Works and People Housing, Bandung, 2017, pp. 1-376 (in Indonesian).

[13] Koulakov I., Yudistira T., Luehr B. G., and Wandono, P, S Velocity and VP/VS Ratio beneath the Toba Caldera Complex (Northern Sumatra) from Local Earthquake Tomography, Geophys J Int, vol. 177, no. 3, 2009, pp. 1121–1139.

[14] Burbank D. W., and Anderson R. S., Tectonic Geomorphology - 2nd Ed., John Wiley & Sons, Chichester, 2012, pp. 1–454.

[15] Natawidjaja D. H., Major Bifurcations, Slip Rates, and A Creeping Segment of Sumatran Fault Zone in Tarutung-Sarulla-Sipirok-Padangsidempuan, Central Sumatra, Indonesia, Indonesian Journal on Geoscience, vol. 5, no. 2, 2018, pp. 137–160.

[16] Aldis D. R., Handoyo R., Ghazali S. A., and Kustono, Geological Map of Sidikalang and (Part of) Sinabang, Sumatra, Geological Survey Center, Geological Agency, 2011 (in Indonesian).

[17] Cameron N. R., Aspden J. A., Bridge D. M. C., Djunuddin A., Ghazali S. A., Harahap H., Hariwidjaja, Johari S., Kartawa W., Keats W., Ngabito H., Rock N. M. S., and Whandoyo R.,

Geological Map of Medan Sheet, Sumatra, Centre for Geological Survey, Geological Agency, 1982 (in Indonesian).
[18] Clarke M. C. G., Ghazali S. A., Harahap H., Kusyono, and Stephenson, Geological Map of the Pematang Siantar Sheet, Sumatra, Geological Survey Centre, Geological Agency, 2011 (in Indonesian).
[19] Aspden J. A., Kartawa W., Aldiss D. T., Djunuddin A., Diatma D., Clarke M. C. G., Whandoyo R., and Harahap H., Geological Map of Padangsidempuan and Sibolga Sheets, Sumatra, Geological Survey Centre, Geological Agency, 2007 (in Indonesian).
[20] Indonesia Geospatial, Information Systems and Remote Sensing, 2023, https://www.indonesia-geospasial.com (in Indonesian).
[21] Geospatial Information Agency (BIG), National Seamless Digital Elevation Model (DEM) and Bathymetry (DEMNAS), 2023, https://tanahair.indonesia.go.id.
[22] Barber A. J., Crow M. J., and Milsom J. S., Sumatera: Resources and Tectonic Evolution, Geological Society Memoirs, vol. 31, London, 2005, pp. 1–282.
[23] Quantum Geographic Information System (QGIS), QGIS Software, 2023, https://www.qgis.org.
[24] Regulation of the Minister of Public Works, Regulation of the Minister of Public Works No. 41/PRT/M/2007 Guidelines for Technical Criteria for Cultivation Areas, Department of Public Works, 2007, pp. 1-43 (in Indonesian).
[25] Zhou Q., Feng W., Song S., Yuan L., and Zhou W., Remote Sense and GIS-Based Division of Landslide Hazard Degree in Wanzhou District of the Three Gorges Reservoir Area, Wuhan University Journal of Natural Sciences, vol. 11, no. 4, 2006, pp. 780–786.
[26] Marliyani G. I., Arrowsmith J. R., and Whipple K. X., Characterization of Slow Slip Rate Faults in Humid Areas: Cimandiri Fault Zone, Indonesia, J Geophys Res Earth Surf, vol. 121, no. 12, 2016, pp. 2287–2308.
[27] Wesnousky S. G., Predicting the Endpoints of Earthquake Ruptures, Nature, vol. 444, no. 7117, 2006, pp. 358–360.
[28] Marliyani G. I., Rockwell T. K., Onderdonk N. W., and McGill S. F., Straightening of the Northern San Jacinto Fault, California, as Seen in the Fault-Structure Evolution of the San Jacinto Valley Stepover, Bulletin of the Seismological Society of America, vol. 103, no. 3, 2013, pp. 2047–2061.
[29] International Seismological Centre (ISC), ISC Bulletin: Event Catalogue Search, 2023, http://www.isc.ac.uk/iscbulletin/search.
[30] Bratt S. R., and Nagy W., The LocSAT Program, Science Applications International Corporation (SAIC), San Diego, California, 1991.
[31] Muksin U., Arifullah A., Simanjuntak A. V. H., Asra N., Muzli M., Wei S., Gunawan E., and Okubo M., Secondary Fault System in Northern Sumatra, Evidenced by Recent Seismicity and Geomorphic Structure, J Asian Earth Sci, vol. 245, 2023.
[32] Waldhauser F., HypoDD--A Program to Compute Double-Difference Hypocenter Locations, U.S. Geol. Survey, 2001.
[33] Waldhauser F., and Ellsworth W. L., A Double-Difference Earthquake Location Algorithm: Method and Application to the Northern Hayward Fault, California, Bulletin of the Seismological Society of America, vol. 90, 2000, pp. 1353–1368.
[34] Cesca S., and Heimann S., Title A Practical on Moment Tensor Inversion Using the Kiwi Tools, GFZ German Research Centre for Geosciences, 2013.
[35] Heimann S., A Robust Method to Estimate Kinematic Earthquake Source Parameters (Ph.d Thesis), University of Hamburg, 2011, pp. 1–161.
[36] Cesca S., Heimann S., Stammler K., and Dahm T., Automated Procedure for Point and Kinematic Source Inversion at Regional Distances, J Geophys Res Solid Earth, vol. 115, no. 6, 2010.
[37] Kennett B. L. N., and Engdahl E. R., Traveltimes for Global Earthquake Location and Phase Identification, Geophys. J. Int., vol. 105, 1991, pp. 429–465.
[38] Gunawan E., An Assessment of Earthquake Scaling Relationships for Crustal Earthquakes in Indonesia, Seismological Research Letters, vol. 92, no. 4, 2021, pp. 2490–2497.
[39] Cheng J., Rong Y., Magistrale H., Chen G., and Xu X., Earthquake Rupture Scaling Relations for Mainland China, Seismol. Res. Lett. 91, vol. no. 1, 2020, pp. 248–261.
[40] Ekström G., Nettles M., and Dziewonski A. M., The Global CMT Project 2004-2010: Centroid-moment Tensors for 13,017 Earthquakes, Phys. Earth Planet. Inter., vol. 200–201, 2012, pp. 1–9.
[41] Ekarsti A. K., Pramumijoyo S., Marliyani G. I., Setianto A., and DwikoritaKarnawati, Analyzing Recent Seismic Activity of The Opak Fault System in Central Java, Indonesia, From 2009 To 2021, International Journal of GEOMATE, vol. 25, no. 110, 2023, pp. 87–97.